A numerical study on droplet-particle collision dynamics

Ilias Malgarinos[1], Nikolaos Nikolopoulos[1,2] and Manolis Gavaises[1]
1: School of Mathematics, Computer Science & Engineering, City University London, Northampton Square, EC1V 0HB London, UK, *Corresp. Author – e-mail: Ilias.Malgarinos.1@city.ac.uk
2: Centre for Research and Technology Hellas, Chemical Process and Energy Resources Institute, Egialeias 52, Marousi, Athens, Gr-15125, Greece

Abstract

The impact of liquid droplets onto spherical stationary solid particles under isothermal conditions is simulated. The CFD model solves the Navier-Stokes equations in three dimensions and employs the Volume of Fluid Method (VOF) coupled with an adaptive local grid refinement technique able to track the liquid-gas interphase. A fast-marching algorithm suitable for the quick computation of distance functions required during the grid refinement in large 3-D computational domains is proposed. The numerical model is validated against experimental data for the case of a water droplet impact onto a spherical particle at low We number and room temperature conditions. Following that, a parametric study is undertaken examining (a) the effect of Weber number ($=\rho u^2 D_o/\sigma$) in the range of 8 to 80 and (b) the droplet to particle size ratio ranging in-between 0.31 and 1.24, on the impact outcome. This has resulted to the identification of two distinct regimes that form during droplet-particle collisions: the partial/full rebound and the coating regimes; the latter results to the disintegration of secondary satellite droplets from elongated expanding liquid ligaments forming behind the impinging droplet. Additionally, the temporal evolution of variables of interest, such as the maximum dimensionless liquid film thickness and the average wetting coverage of the solid particle by the liquid, have been quantified. The present study assists the understanding of the physical processes governing the impact of liquids onto solid spherical surfaces occurring in industrial applications, including fluid catalytic cracking (FCC) reactors.

Keywords: VOF; impingement; droplet; particle; collisions; local refinement

Nomenclature

Acronyms		V	Volume (m^3)
CFD	Computational Fluid Dynamics	$We=\rho_{liq}u_0^2D_0/\sigma$	Weber number (-)
cpR	Cells per Radius (cells that cover the drop radius)	$\vec{x}(x,y,z)$	Position vector [x,y,z-axis distance (m)]
DTP	Droplet To Particle size ratio	Greek letters	
FCC	Fluid Catalytic Cracking	α	Liquid volume fraction (-)
UDF	User defined Function	θ	contact angle (°)
VOF	Volume of Fluid Method	μ	dynamic viscosity (kg/ms)
Symbols		ρ	Density (kg/m^3)
A	Area (m^2)	σ	surface tension coefficient (N/m)
$Bo=\Delta\rho gDo^2/\sigma$	Bond number (-)	τ ($=tu_o/D_o$)	Dimensionless time (-)
C_p	Pressure coeff. (-)	Ω	Computational domain
D	Diameter (m)	*Subscripts*	
d	Distance (m)	C	cell
$Fr = U_o / \sqrt{gD_o}$	Froude number (-)	gas	gas
H	Liquid Film Thickness (m)	liq	liquid
$\hat{n}(\hat{n}_x,\hat{n}_y,\hat{n}_z)$	Free-surface unit normal (-)	m	mean
P	Pressure (Pa)	max	maximum
R	Radius (m)	mom	refers to the momentum equation
$Re=\rho_{liq}u_0D_0/\mu_{liq}$	Reynolds number (-)	o	initial condition
$St = \rho_{liq}R_oU_o/\mu_{gas}$	Stokes number (-)	P	point
t	time (s)	p	particle
$\vec{u}$ (u,v,w)	Velocity (its components) (m/s)		

1. Introduction

The dynamics of droplet impingement onto solid surfaces is realised in many engineering applications, as for example, spray cooling, spray coating, fuel injection in internal combustion engines, fire suppression, inkjet printing, metallurgy and electronic circuits cooling among other. Comprehensive reviews and important numerical and experimental works on droplet impingement onto solid flat surfaces for isothermal and non-isothermal conditions have been presented (selectively) by [1-4]. The main parameters affecting similar phenomena are clearly identified as those of a) the nature of the impinging surface, (solid surface roughness, wettability), b) the liquid and gas properties, c) the temperature of the surface, d) the impact velocity, and e) the droplet diameter. Selective experimental studies, where these parameters are investigated are presented in [1, 5, 6]. The outcomes range from spreading and relaxing, to rebounding and splashing, while it becomes more complex for impingement on hot and/or rough surfaces [7].

However, unlike droplet impingement onto solid flat surfaces, very little concrete experimental and verified numerical information is available for droplet impact onto non-flat spherical surfaces and especially for droplet-particle collisions. A review of the relevant works (experimental and numerical) on this subject starts since 1971, when Levin and Hobbs [8] published the first (to the best of the authors knowledge) experimental work on droplet impingement onto a spherical surface, under the effect of gravity, where the regime of the impingement included droplet splashing. In 1999, Hardalupas et al. [9] also studied droplet splashing onto spherical targets.

More recently, in 2003, Gunjal et al. [10] used the VOF methodology in 2D computational domains, in order to simulate the liquid shape formations after the off-center impingement of a liquid droplet onto a spherical surface, using experimental data from own experimental campaigns. However, the simplification of the phenomenon in two dimensions (planar) was not enough for the accurate representation of the physics that lie behind this asymmetric impingement.

In 2007, Bakshi et al. [11] performed experiments for the coating of a spherical solid particle by a droplet of similar size. This was one of the first studies, where the droplet to particle size ratio was close to unity and therefore, the “coating” outcome could be observed. The authors also presented an analytical model for the prediction of droplet spreading and presented results for the thickness of the liquid film at the impact side. During the same year, Ge and Fan [12] presented Level-Set simulations and experiments on droplet impact on a spherical particle of similar size, in the Leidenfrost regime. In 2009, Bangonde et al. [13] presented VOF simulations and experiments at low Weber number droplet impingement on a cylindrical pipe, followed also by the case of impact on a spherical surface. In 2012, Gac and Gradon [14] used the Lattice-Boltzmann method to simulate the phenomenon and categorized the collision outcomes in three regimes, i,e, coalescence, ripping and coating (1-5 satellite droplets) and skirt-scattering, based on the initial droplet Weber number. The authors observed that the outcome scenarios don’t change significantly with other solid target shapes (cubical, ellipsoidal). Their work was purely numerical, i.e. no validation with experiments was presented. Moreover, the effect of droplet to particle size ratio was not explicitly investigated, as the authors differentiated collision outcomes based only on the impact Weber number. In 2013, Mitra et al. [15] presented simulations and experiments on droplet impingement onto a spherical particle, under isothermal and non-isothermal conditions. In their work, they focus more on the effect of particle temperature on the solid-liquid contact and not on quantifying the collision outcomes. Finally, in 2014, Zhang et al. [16] presented Lattice-Boltzmann Method (LBM) based simulations on droplet impact onto a spherical particle for low Reynolds and Weber numbers and moderate liquid to air density ratio. The authors investigated the effect of We and droplet-particle size ratio parameters on the outcome; however they only studied low Weber numbers (up to 26.14) which are below the threshold for different impact regimes to be realised. The authors also compared the non-

dimensional film thickness at the impact side predicted from CFD against the correlations given in [11]. As it seems, studies concerning droplet-particle collisions are limited. A parametric study on the effect of droplet-particle size ratio for a wider range of Weber number of impact has not been presented, although it is needed for establishing collision outcome maps. The present study aims to fill this gap; it examines different types of collisions using CFD analysis that distinguish the impact outcome of influential parameters, such as the We number and the droplet-particle size ratio. The effect of wettability is not included in the current study as there is no experimental information regarding the contact angle values experienced during these impacts; moreover, performing further parametric studies that would examine the effect of wettability would significantly increase the computational effort. Despite that, the investigation of such phenomena may contribute to the understanding of similar processes happening in technological applications, such as for example FCC reactors used in petroleum industry in order to convert heavy hydrocarbon droplets into lighter gas products. However in the present work, the assumptions of stationary particles and the inclusion of gravity, which may not be directly relevant to FCC conditions, were mainly adopted for the validation of the proposed methodology against experimental measurements and relevant numerical works.

2. Numerical method

The numerical model used in the present paper is based on a previous work of the authors [17], where it was used to simulate the droplet impact onto solid flat surfaces under isothermal conditions for a wide range of operating conditions. For completeness, in the following section, a short introduction on the basic principles of the CFD model utilized is presented, followed by the description of the advancements made here in the dynamic local grid refinement model.

2.1 Fluid Flow and Volume of Fluid Method (VOF)

The CFD model utilized In this work includes the solution of the Navier-Stokes equations for the prediction of fluid flow, while the liquid-gas interphase is tracked using the Volume of Fluid Method (VOF) [18]. The equations are solved in the commercial software ANSYS FLUENT [19]. In [17], a dynamic local grid refinement technique was implemented using User Defined Functions (UDFs) for resolving in high detail the liquid-gas interphase throughout the liquid deformation. By utilizing this technique, computational time was saved compared to a uniform refined grid having the same resolution. Technical details of the model utilised follow. For the more accurate calculation of the liquid-gas interface curvature, the unit surface normal vectors at the computational nodes are used. Pressure–velocity coupling is achieved by the PISO algorithm. Discretization of the momentum flux term is achieved by a second order upwind scheme, while for the time discretization a first-order implicit approach is followed for the momentum equation. The volume fraction equation is solved in an explicit manner at the beginning of each time-step using as an input the velocity values derived during the previous time step. For the volume fraction flux term, the CICSAM [20] discretization scheme is used. CICSAM has been proved to be a reliable tool for the prediction of various two-fluid phenomena as presented in previous works [21-23] [24-28] of the authors and their co-workers. For the implementation of the contact angle on the spherical surface, the same method used for the flat wall case is followed [17] considering that the advancing and receding angles are constant. In such a case, the normal to the interface unit vector at the wall boundary cells is prescribed, according to the predefined value of the contact angle θ.

2.2 Advancement in local refinement technique

The refinement algorithm which was used in [17] is extended in the present study so as to include different

distances between the refinement levels, as shown in Figure 1. The proposed algorithm allows for the interface to be enclosed within a dense region of computational cells. In this work, a region of approximately 14 cells along the interface normal direction is used, as depicted in Figure 1.

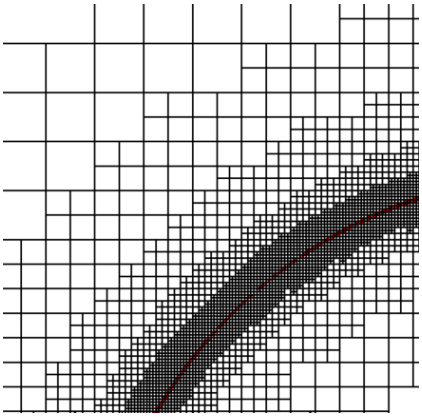

Figure 1. Local refinement algorithm**.** Specific width is given for each level of refinement.

The procedure executed for the refinement technique is described here. At first, a fast marching algorithm (presented in the following section) is executed in order to quickly calculate the minimum distance of each computational cell from the interface (distance function). Then, based on this distance function and the desired width of each refinement level region, the cells are set to be refined/coarsened.

Refinement/coarsening procedure is executed as many times as the maximum number of refinement levels, while the cells are refined progressively from the lowest to the highest level of refinement and coarsened towards the opposite direction. It is important to notice that during the grid adaption procedure, refinement/coarsening is only executed once for each cell, meaning that one refinement level up/down is performed, thus avoiding problems that may arise when parent cells which lie in the bounding limits of parallel processor domain regions need to be coarsened from one side and refined from the other.

A typical example of the implemented local refinement algorithm is presented in Figure 2. As the droplet spreads on the particle surface, the grid is refined at the area of interface, while also on the interface between liquid and entrapped air.

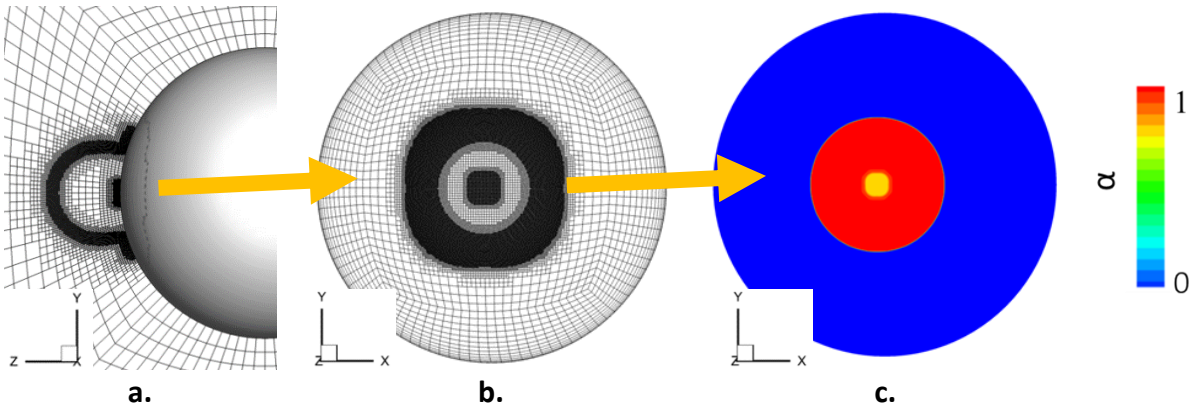

Figure 2. Demonstration of the grid refinement algorithm. The grid follows the motion of the droplet interface. The air bubble formed at the impact point is also resolved; (a) side view, (b) top view and (c) volume fraction contour on wall surface (τ=0.26, We=80, DTP=0.31).

2.3 Fast-marching algorithm for the computation of iso-surfaces

The demand for an accurate and quick approximation of a distance function in relation to the interface location, is dictated by the local refinement algorithm. In [17], the minimum distance of each cell to the interface was calculated in a straightforward fashion as:

$$d = \min\left|\vec{x} - \vec{x}_{\text{int}}\right|, \vec{x}(x,y,z) \in \Omega \quad (1)$$

where Ω stands for the computational domain. The number of cell loops required for this calculation *was proportional to the product of interface cell count multiplied by the domain cell count* O(interphase cells*domain cells); the resulting number may grow enormously in 3-D simulations. Moreover, when this method is applied simultaneously with parallelization, the algorithm becomes inevitably time consuming. This is because there is no link between the geometrical locations of the parallel processor grid regions and the location of the liquid-gas interface, thus data exchange between all processors is executed so that the minimum distance to the interface can be computed in each processor.

In order to overcome these limitations, an algorithm similar to the work of Elias et al. [29] which was developed for finite elements is implemented in this work; this algorithm calculates the distance function from the interphase faster. The calculation of the distance function starts from the interface cell points (nodes) and then continues to neighboring cells/points along the direction of the interface normal unit vector $\hat{n}$. The advantage of this method is that only neighboring grid region processors have to exchange point data, instead of data exchange between all processors, as required by eq 1. This fast-marching algorithm is presented schematically in Figure 3 and its basic three steps are summarized below:

1) A cell loop is initially performed and the interface cells (those defined by the α=0.5 iso-surface) are identified. For these cells, a cell point loop is then executed and *the minimum distance from the interface is calculated and stored at each point*. Vector $\hat{n}$ is copied from the cell centre to the points, while the cells used and all their points are flagged as visited.
2) A second cell loop is performed. *If at least one point inside any cell is flagged as visited, then the distance from the interphase in the cell centre is calculated* using the visited point value as (notation presented in Figure 2b):

   $$d_C = \overrightarrow{CP} \cdot \hat{n} + d_P \quad (2)$$

   If more than one points are flagged as visited in the cell, the minimum distance value from all point calculations is kept. Vector $\hat{n}$ is copied from the points to the cell centre, while the cells used and all their points are flagged as visited.

3) Finally, a third cell loop is performed. *If a cell is already visited*, without having all of its points visited, *the distance from the interface is calculated in all the cell points* using this time the value at the cell centre:

   $$d_P = \overrightarrow{CP} \cdot \hat{n} + d_C \quad (3)$$

   In this step, whenever a point is already visited, the minimum of the previously stored value and the newly calculated one is kept.

Steps 2 and 3 are repeated until all cells of the domain have been filled in with a distance value. The three steps of the algorithm are shown in Figure 3a, while in Figure 3b the notation used in eq. 2, 3 for the local calculation of the minimum distance from the interface is indicated.

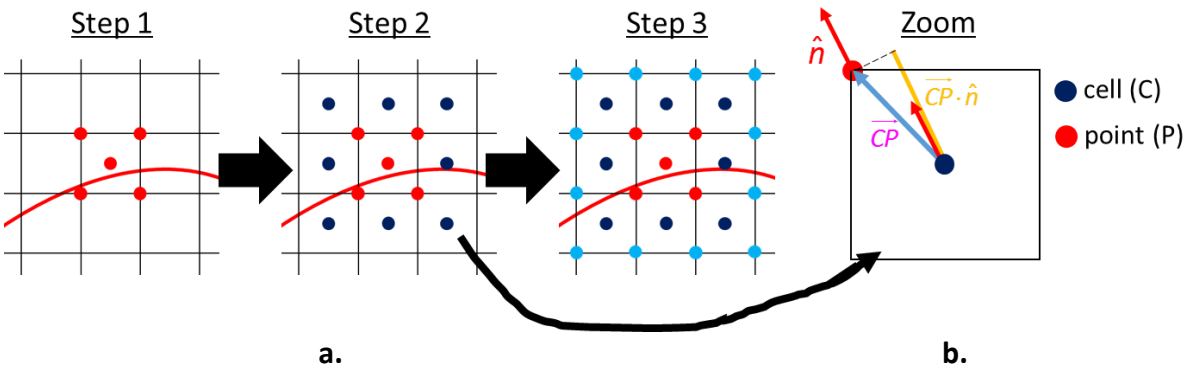

Figure 3. a) Schematic representation of the fast marching algorithm steps to calculate distance function starting from a single cell; step 1: red, step 2: blue and step 3: light blue. b) Calculation of the distance function at a random cell located far from the interface.

Due to the copying of interface unit vector from cell centres to points and vice-versa, the calculation of distance function is executed on a local basis, thus cell alignment and marching direction affect accuracy. However, this method gains in computational time, as the number of *cell loops that are performed are proportional to the number of cells marched in the normal direction to the interface* O(interphase cells*marching cells along normal to interphase), which is significantly smaller than the previously reported method (eq. 1), especially in large computational domains.

3. Simulation cases

As a reference case for the validation of the numerical model, the work of Mitra et al. [15] is used, where experiments with water droplets impacting onto a larger spherical solid cup at room temperature, under the effect of gravity have been reported. In their work, they also presented ANSYS/FLUENT simulations for a very low Weber number, while they used either a static contact angle of 90° or a dynamic one. The dynamic contact angle was changing with time, based on experimentally measured data; this allowed the numerical model to predict better the temporal evolution of the phenomenon, compared to the static contact angle simulations, as also shown in other works for dynamic contact angle models [17, 30, 31]. However, no specific values of advancing/receding representative dynamic contact angles have been reported. Contact angle values are function of the specific liquid and solid material used and the surface properties, and affect the impact outcome. However, in the present study we have concentrated only on the effect of We number and droplet-to particle size ratio (DTP) on the impact outcome neglecting the variation of contact angle, which has been kept constant to 90°. Despite that, to the best of the authors' knowledge, such a parametric study is not yet available in the open literature, as already mentioned in the introduction section.

The details of all cases examined in the current study are presented in Table 1. The first two cases (1, and 1a) were used in order to estimate the grid dependency of the numerical results and to validate the numerical model. The remaining 8 cases refer to the parametric studies conducted. In all cases, the size of the droplet remained unchanged. The effect of DTP on the collision outcome was investigated by changing the size of the solid particle by half and one-fourth of its initial size. Weber numbers of 8, 40 and 80 were examined. Gravity was applied towards the z direction, as in the experimental study used for the model validation (Case1). Bond number which expresses the relation of gravity and surface tension forces is 1.3 for all cases, while Froude number which quantifies the relation of inertial forces to gravity ranges in between 2.5-7.9, thus revealing that gravity force is of significance for the induced droplet dynamics for the range of parameters investigated in this study.

Case No.	u_0 (m/s)	D_0 (mm)	D_p (mm)	DTP	θ (°)	We	Re	Refin. Lev	cpR
1	**0.434**	3.1	**10**	**0.31**	90	**8**	1336	4	52-82
1a	0.434	3.1	10	0.31	90	8	1336	5	104-164
2	**0.97**	3.1	10	0.31	90	**40**	2987	4	52-82
3	**1.372**	3.1	10	0.31	90	**80**	4224	4	52-82
4	0.434	3.1	**5**	**0.62**	90	8	1336	3	52-82
5	0.97	3.1	5	0.62	90	40	2987	3	52-82
6	1.372	3.1	5	0.62	90	80	4224	3	52-82
7	0.434	3.1	**2.5**	**1.24**	90	8	1336	2	52-82
8	0.97	3.1	2.5	1.24	90	40	2987	2	52-82
9	1.372	3.1	2.5	1.24	90	80	4224	2	52-82

Table 1. Simulated Cases for droplet-particle collisions.

The physical properties for the water and air used were ρ_{liq}=998.2 kg/m^3, ρ_{gas}=1.225 kg/m^3, μ_{liq}=0.001003 kg/ms, μ_{gas}=1.78E-05 kg/ms and σ=0.0728 N/m. The Courant number was kept constant throughout the solution and equal to 0.25, by updating at every time iteration the solution time-step. The latter was in the range of 1μs, whilst the equations were considered as being converged for a dimensionless residual less than 1.E-06.

The number of grid refinement levels was chosen so that the accuracy in all cases can be almost the same, despite the fact that the particle size changed. The resulting cpR number varies, because the grid is not uniform as it is shown in the following section.

The inclusion of turbulence effects is not expected to play a role in the cases studied in the present work. As it is mentioned by Pasandideh et al. [32], droplet impingement onto a flat surface having a Re in the order of 10^4 is "too small to induce turbulence" and thus the liquid phase flow over a flat plate after droplet impact, can be regarded as a laminar one. In this study, the Reynolds number used lies in the range of 1336-4224, thus falls into the laminar regime proposed by [32]. Moreover, to the best of authors' knowledge, there are no studies of turbulence effects induced during the impact of a droplet onto a solid target of any shape. Most numerical papers that try to simulate the phenomenon do not account for turbulence effects irrespective of the grid size they use [22, 32-34]. The minimum cell size in this work is 18.9μm, based on the maximum cpR of 82 used at the proximity of the particle surface. The Kolmogorov length scale (n), is equal to $n=(\nu^3/\varepsilon)^{1/4}$, taking as an estimation for turbulent kinetic energy (ε) a value of ~U^3/D. For the cases presented in this study, n is approximately equal to 28.4μm for the gas, as calculated using the initial values of U_o, D_o. It is obvious that the gas phase turbulent structures, if any, are adequately resolved. Finally, the Kolmogorov time scale, which is equal to $\tau_n=(\varepsilon/\nu)^{1/2}$, lies in the range of 3.5e-05, 9.9e-05 s; this is resolved by the timestep applied (1e-06).

Finally, based on the cell size used, detailed secondary phenomena which have been reported in literature as the air bubble sheet entrapped during the initial stage of impingement (1-2.5μm) [35, 36], cannot be resolved. The controlling parameter for air entrapment is the Stokes number, which for the current cases ranges in-between approximately 3.8e+04 - 1.2e+05 ($St = \rho_{liq}R_oU_o/\mu_{gas}$ from [36]). This means that the dimple height, i.e. the thickness of the region where the liquid has been deformed into a dimple shape due to the pressure build-up at impact point, is around 0.6-1.4μm from [35, 36], which is much smaller than the currently applied grid size, i.e. almost twenty (20) times less. To resolve such a thickness with an acceptable accuracy one should apply almost 25 refinement levels turning in an increase of the associated computational cost by a range of 8^{20}. However in this work, and most possibly owed to the fact that the grid resolution is not high enough to capture the bubble dynamics in high detail, the entrapment of one big bubble at impact point is captured using the current grid sizing, as shown in Figure 2c.

3.1 Computational domain – Boundary conditions

Due to the fact that the particle diameter was varying, different grids were used for each case. All applied numerical grids contained only hexahedron cells, while the grid lines were designed to start from the spherical particle and expand spherically in the flow domain (Figure 4). This choice resulted in varying cell size, as shown in Figure 4. To reduce the computational cost, half of droplet was simulated, since the phenomenon can be regarded as almost symmetrical. For Case 1a it is known from Mitra et al. [15] that the droplet rebounds after impinging on the solid particle; thus, the computational domain was restricted to the one fourth of the particle (Figure 4a). The computational grid for all other cases is presented in **Figure 4**b. This domain includes both the collision side as well as its wake side (downstream the main flow direction, behind the spherical particle).

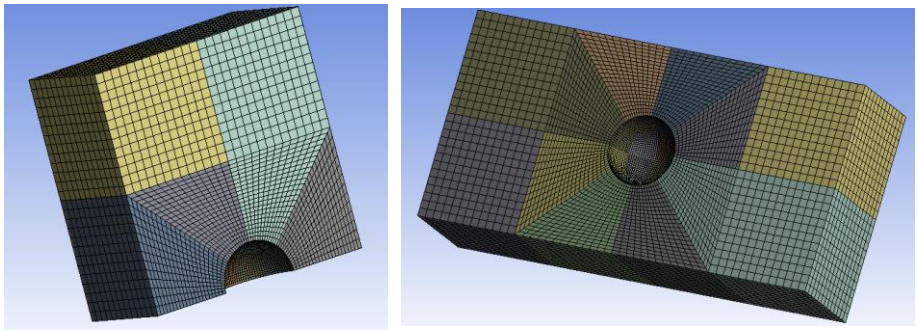

a. **b.**

Figure 4. Computational grid used for a) the validation Cases 1,1a and b) Cases 2-9.

It should be mentioned that the cell skewness located at the proximity of the four diagonal grid lines is owed to the specific method followed for the grid construction; this affects the advection of volume fraction during the time instants when the liquid thickness becomes similar to the cell width in this area. The particle circumference was discretised with the same number of cells (104 cells) for all cases. This was considered accurate enough to resolve the spherical particle shape. Based on the fact that the particle diameter was reduced by a factor of 0.5 in cases 1-3, 4-6 and 7-9, and the fact that when using the refinement algorithm one cell edge is split in two edges, the same grid sizes were achieved for all particle sizes, using always one less level of refinement for every particle diameter decrease (Table 1). In Figure 5, the cell size at the vicinity of liquid-solid interface is shown to be similar for all cases examined, except for case 1a, which acts as the validation of the applied numerical algorithm.

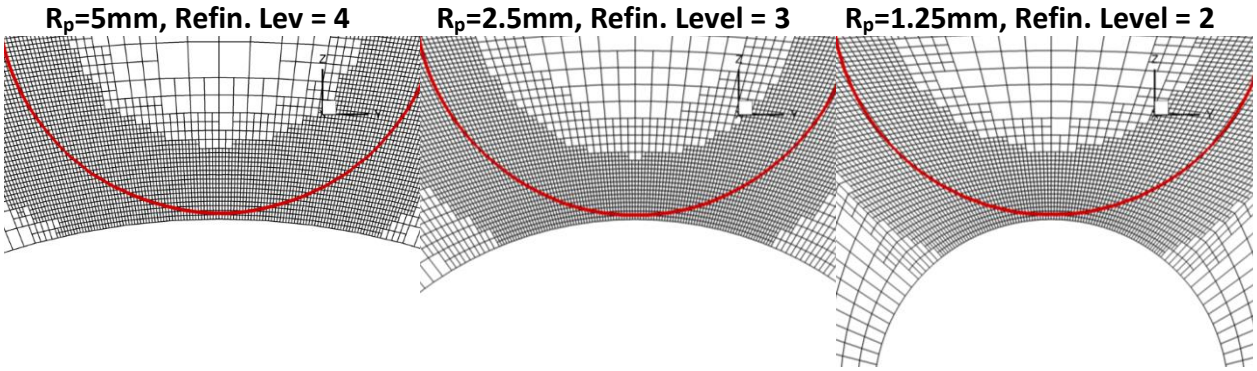

Figure 5. Particle diameter changes but cell width close to particle remains the same for all cases (ex in left picture, $2\pi R_p/104/2^{levelsofRef}$=18.9 μm) by using less levels of refinement. (τ=0, left: cases1-3, middle: cases4-6, right: cases 7-9)

The boundary conditions applied for all cases examined are presented in Figure 6. The solid particle is represented by a spherical wall, while a symmetry plane along the direction of the droplet motion is applied. All remaining boundary conditions were set as open boundaries. In all cases examined, the droplet was initially placed at a distance of one droplet diameter away from the spherical particle, allowing for the induced flow field prior to impact to develop.

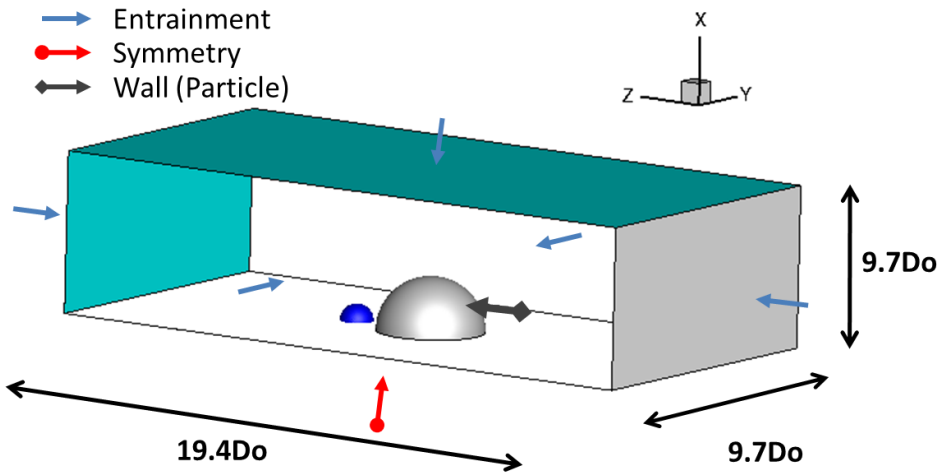

Figure 6. Computational domain along with the applied boundary conditions.

Information relevant to the computational resources required for the runs performed is presented in Table 2.

Cases	Coarse grid (mill cells)	Initial grid (mill cells)	Maximum grid (mill cells)	Processors	Time elapsed (days)	Uniform equiv. grid (mill cells)
1-3	0.051	0.183	1.55-2.45	12	15	208
4-6	0.19	0.257	0.9-1.55	12	10	97
7-9	0.363	0.469	1.04-1.1	12	5	23

Table 2. Number of cells and simulation times for all runs performed.

4. Results and Discussion

4.1 Reference case-Droplet rebound

Figure 7 presents the numerical results of the first two cases presented in Table 1. In Figure 7a the spreading diameter as calculated by the present CFD simulations is presented. The derived numerical results, after using 4 and 5 levels of local refinement for cases 1 and 1a, respectively, are depicted and compared against the corresponding experimental data and simulations performed by Mitra et al. [15] in Figure 7b. The trend of the results indicates that as the grid cell size becomes smaller, the results can be regarded as more accurate. Moreover, the current model results approach better the experimental data in comparison with the corresponding Mitra et al. simulations; of course when Mitra et al. applied the

dynamic contact angle variation as measured during the experimental campaigns, their results were significantly improved and the derived droplet spreading line is as well evident in Figure 7.

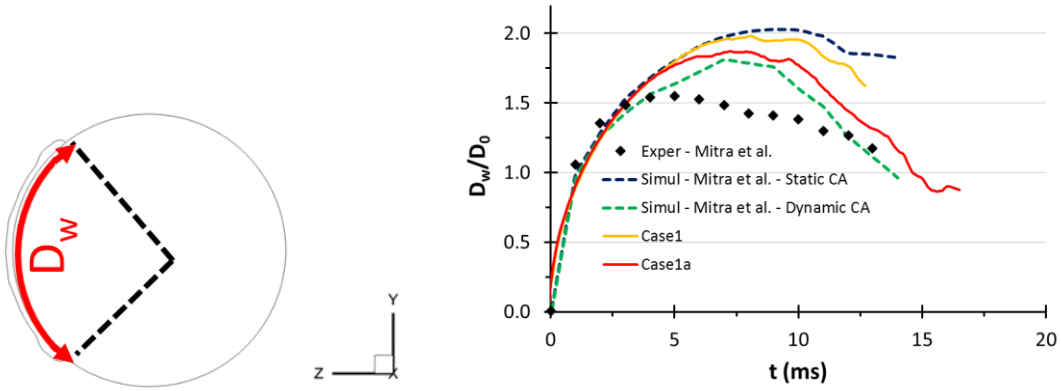

a. b.

Figure 7. a) Spreading diameter D_w definition for spherical particle impacts; b) Temporal evolution of dimensionless droplet spreading diameter compared to experimental data and simulation results taken from Mitra et al. [15].

In Figure 8, the comparison between experimental images and simulation results from [15] along with the results of the current model are presented; they exhibit a good agreement, especially during the recoiling phase. Small differences in the droplet shape are reflected to the over-estimation of droplet maximum spreading, as highlighted in Figure 7, and which can be attributed to the use of a static contact angle instead of the real experienced values. The numerical model gives results within an acceptable level of agreement against the relevant experimental data.

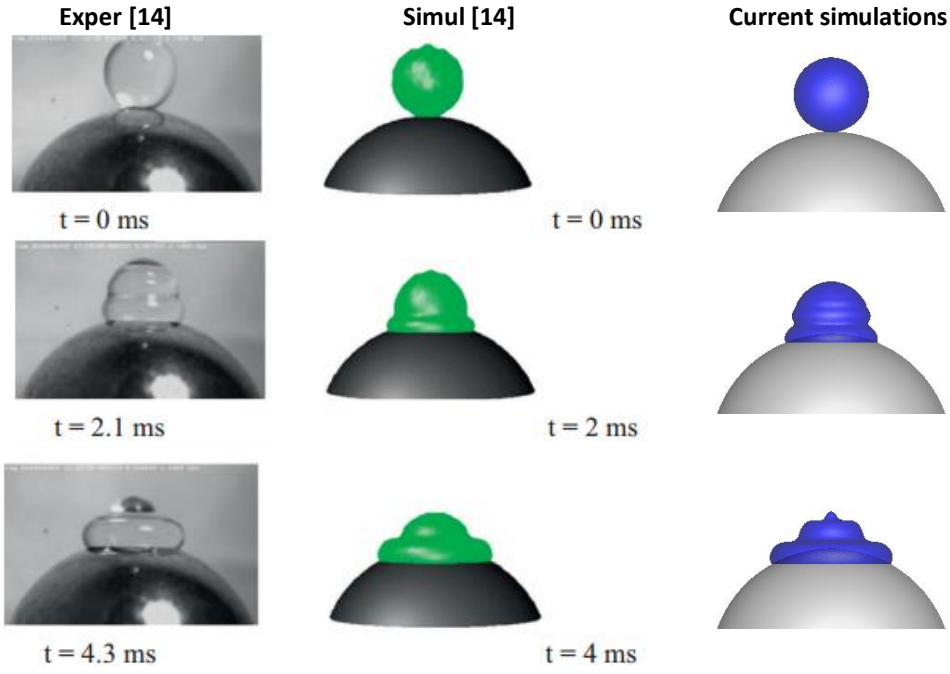

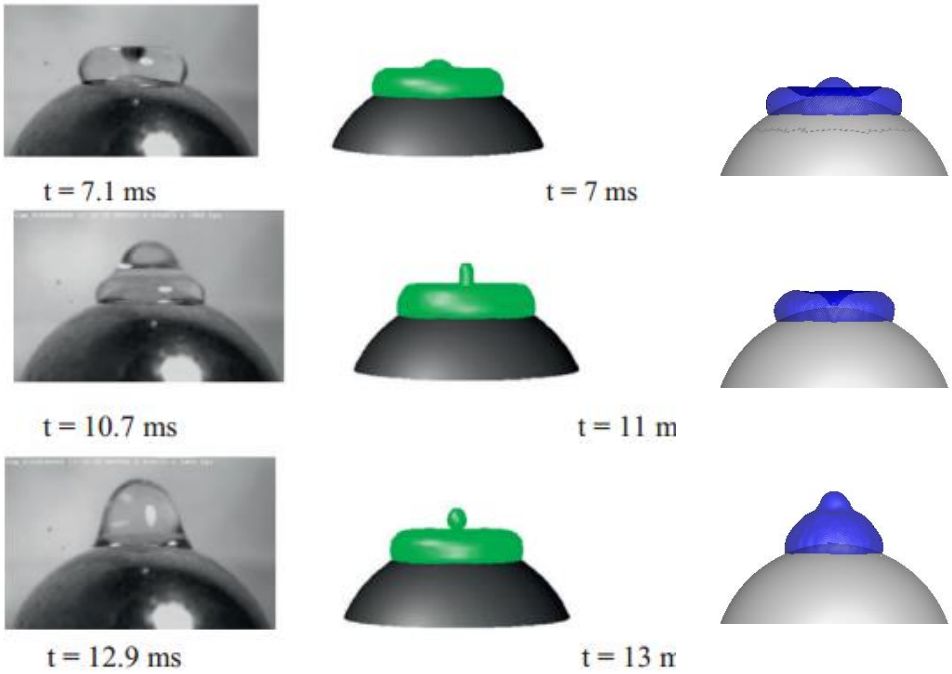

Figure 8. Comparison between experimental photos (left) and simulation results taken from Mitra et al. [15] (centre) with the present simulation results (right).

4.2 Investigation of droplet-particle dynamics for varying DTP and We number.

4.2.1 Hydrodynamics of collision outcomes

After the validation of the numerical model for the case of droplet impingement onto a spherical particle, a parametric study was performed in order to investigate the dynamics of the droplet-particle collisions under different impact conditions. The predicted collision outcomes are grouped and depicted in Figure 9a utilizing representative images for all cases examined. In Figure 9b the two distinctive outcome regimes, namely rebound and coating are separated by a curve. This critical curve results from the observation that coating will take place when the droplet initial kinetic energy is equal or higher than the surface energy needed to spread the film past the particle equator, i.e. when the following ratio equals to unity to derive the limiting curve:

$$\frac{E_{kin}}{E_{0.5surf}} = \frac{m_o u_o^2/2}{\sigma A_{psurf}/2} = \frac{\rho_o u_o^2 \pi D_o^3/12}{\sigma \pi D_p^2/2} = \left(\frac{\rho_o u_o^2 D_o}{\sigma}\right)\cdot\left(\frac{D_o}{D_p}\right)^2 \cdot \frac{1}{6} = We \cdot DTP^2 \cdot \frac{1}{6} \qquad (4)$$

Simulation results for the collision outcome are spread nicely on the two sides of this limiting curve. It can be noticed that in Case3 (DTP=0.31. We=80), where the droplet breaks up after its collision with the solid particle, part of the liquid mass starts sliding downwards, thus marking the threshold from rebound to coating regime.

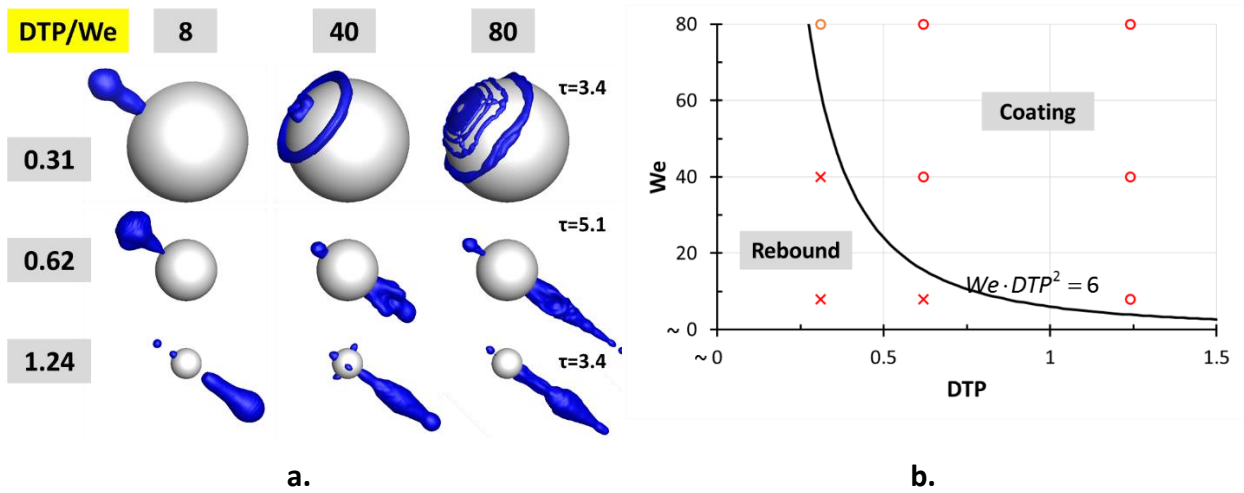

Figure 9. a) Droplet-particle collision outcomes for Cases 1-9. b) We-DTP collision outcome map. Circle, 'x' markers denote coating/rebound regime respectively.

Based on the numerical results, both the increase of DTP as well as that of impact velocity, reinforce the transition from droplet rebound regime to the full particle coating one, for the range of parameters studied here. The consideration of wettability effect is expected to shift the border line on Figure 9b. For example, if hydrophobic impacts are taken into account, this line is expected to be shifted towards higher We numbers for the same DTP, since hydrophobicity promotes rebound over coating.

For droplets of significantly smaller size than the solid particle, as in Cases 1-3, the droplet rebounds after impact. A typical example was shown in Case1 (also presented in Figure 8). During the initial stages of impingement, the droplet spreads onto the spherical surface until the surface tension force overweighs the initial drop kinetic energy and gravitational forces that promote spreading. Viscous dissipation prohibits the liquid free motion in both spreading/recoiling phases. It is obvious that for the cases characterized by small DTP values, droplet-solid interaction resembles the behaviour observed in flat surfaces, namely droplet rebound. In Figure 10 the effect of impact velocity on maximum drop spreading on the solid particle is presented for Cases1-3.

As the impact velocity increases, the droplet spreads more onto the solid particle. For the early stages of the phenomenon, all lines coincide. This behaviour is similar to the droplet impingement onto a flat surface as shown in the work of Rioboo et al. [3], where in the initial kinematic phase all lines coincide and wettability and We are not influential. For the case of moderate Weber number impacts (Cases2, 3 respectively), fragmentation of the liquid film that spreads/retracts on the solid particle is observed. For the moderate Weber number case (Case3) a significant part of the liquid mass starts sliding down towards the downstream side of impact.

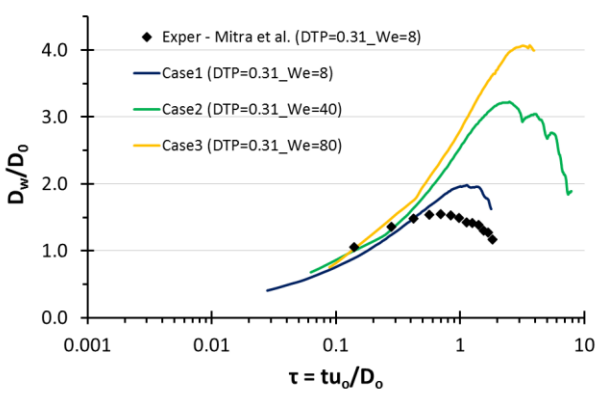

Figure 10. Effect of We number on the dimensionless wetting diameter for Cases 1-3.

In Figure 11 the temporal evolution of the average volume weighted liquid phase velocity along the z-axis (impact axis) is presented for Cases 1-3. The mean velocity is calculated from the following equation:

$$w_m = \frac{\sum_{c,\alpha>0.5} \alpha \cdot V_c \cdot w_c}{\sum_{c,\alpha>0.5} \alpha \cdot V_c} \qquad (5)$$

It is obvious that as the impact velocity increases, the average liquid velocity decreases at a slower rate, implying that it takes longer for the viscous dissipation and surface tension forces to outweigh gravity and initial kinetic energy. For the high Weber number case, the volume weighted velocity is positive throughout the phenomenon, thus showing that a significant part of drop mass continues the sliding motion along the particle surface. This Figure shows that the outcome observed in Figure 9 complies with the mean velocity prediction, minding the fact that it also includes liquid retraction.

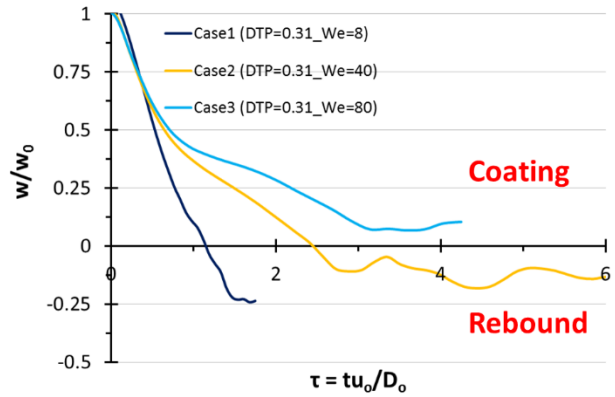

Figure 11. Effect of We number on the liquid phase mean velocity along the drop-particle axis (z direction) for Cases1-3.

Attention is now turned on to cases with higher DTP. In Cases 4-6 the size of the solid particle gets smaller; thus, the transition to particle coating regime is enhanced. In these cases, where drop-particle collisions have a DTP value of 0.62, the Weber number is the decisive parameter. For very low Weber number, the droplet still rebounds from the solid surface, while for higher Weber numbers the droplet coats the particle. A typical example of particle coating is presented in Figure 12 for case 5; the drop surface is

coloured with the non-dimensional velocity magnitude $|u|/|u_o|$. This dimensionless value and is also plotted on the the y=0 plane of symmetry.

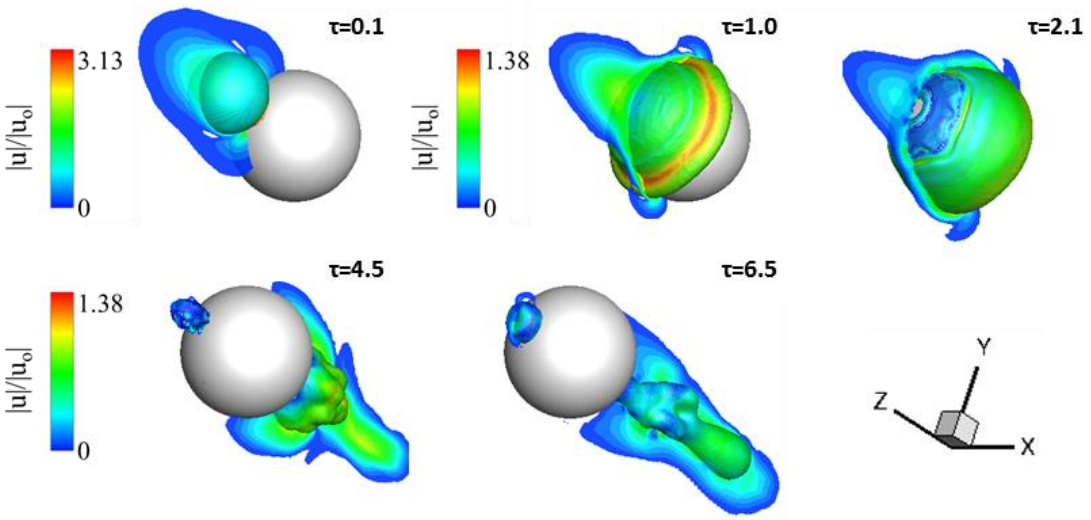

Figure 12. Temporal evolution of drop-particle collision for Case 5 (DTP=0.62_We=40). Drop iso-surface (α=0.5) and slice y=0 coloured by the dimensionless velocity magnitude. Values below 0.15 are cut-off.

The droplet after hitting the solid particle spreads across its surface, up to the point where the liquid film thickness on the particle surface becomes so thin that inevitably breaks (τ=2.1). As soon as the droplet impacts the particle and begins wetting it, inertial and gravitational forces promoting spreading are counterbalanced by liquid viscous and surface tension forces. Break-up occurs when under the simultaneous effect of all these forces, neck areas which are characterized by very small thickness, are developing on the spreading lamella. This physical mechanism is referred as end-pinching mechanism in the open literature and the exact area of neck formation is highly dependent on the induced flow field characteristics, which stretch the liquid phase (lamella) making it very thin at the point of break-up. The exact position of the neck break-up is affected by the applied cell size. This phenomenon can be resolved in various cases (binary droplet collision, droplet impingement onto flat surfaces, [17], [21-23]) by applying in 2D grids a cpR of 72-120. Therefore, for the specific cases examined in this paper, the applied cpR is in the limit of the necessary grid size to reproduce the exact dynamics of the break-up mechanism. In Figure 13, this specific drop breakup mechanism is depicted in more detail. The liquid film becomes so thin that breaks up at some point and then under the influence of surface tension force tends to retract. During this deformation, an internal liquid recirculation is induced within the retracting rim, shown in Figure 13c. This recirculation marks the initiation of the retracting motion of the liquid mass.

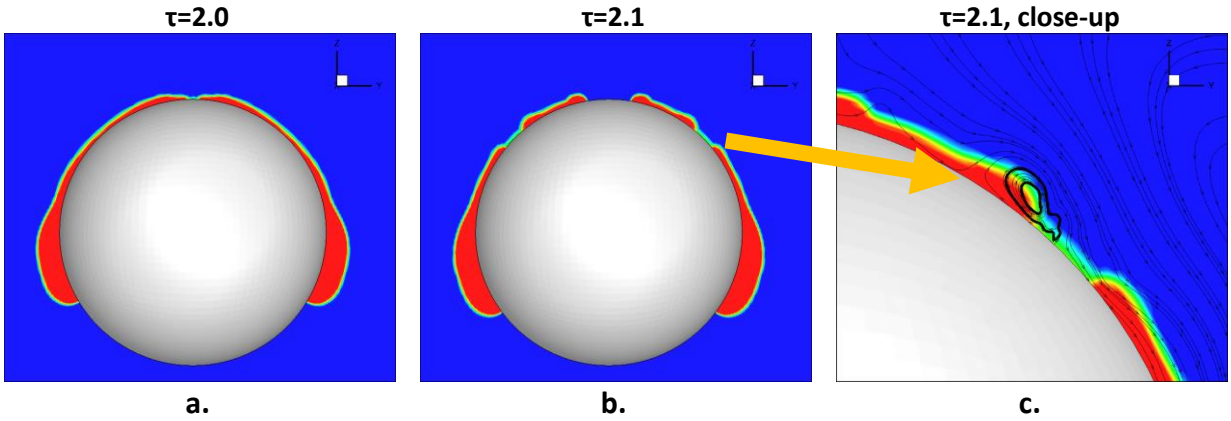

Figure 13. a, b) Evolution of thin film break-up and c) close up view of the break-up region.

After this point, the liquid mass is separated in two distinct parts. The first one retracts on the solid particle surface, while the second one which contains most of the initial droplet mass, continues spreading until it accumulates behind the particle and forms an elongated ligament that leaves the particle surface. This ligament that is moving in the particle wake region may result to a small number of satellite droplets (<=3). As the Weber number increases, the instabilities induced at the liquid flowing away from the particle get more intense and the ligament becomes thinner, as presented in Figure 9.

The coating outcome is summarized in Figure 14, where the following phenomena are observed: (a) particle coating (τ=2), (b) liquid mass accumulation in the particle wake region (τ=6.8) and (c) possible satellite drop injection (τ=9.3).

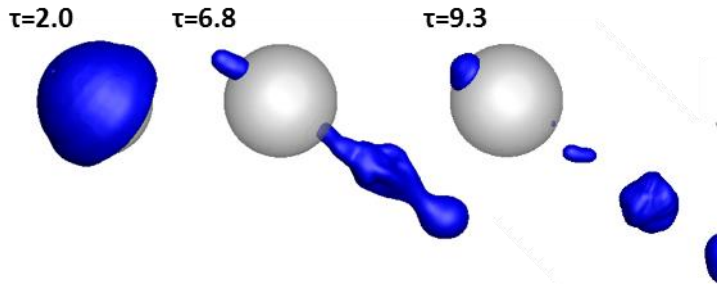

Figure 14. Droplet-particle collision mechanism (coating, mass accumulation and satellite drop formation) shown for Case5 (DTP=0.62_We=40).

The temporal evolution of pressure coefficient C_p is presented in Figure 15 for Case5 at the same time instants as Figure 12. C_p represents a non-dimensional pressure defined as:

$$C_p = \frac{P_{mom}}{1/2\rho_{liq}u_o^2} \quad (6)$$

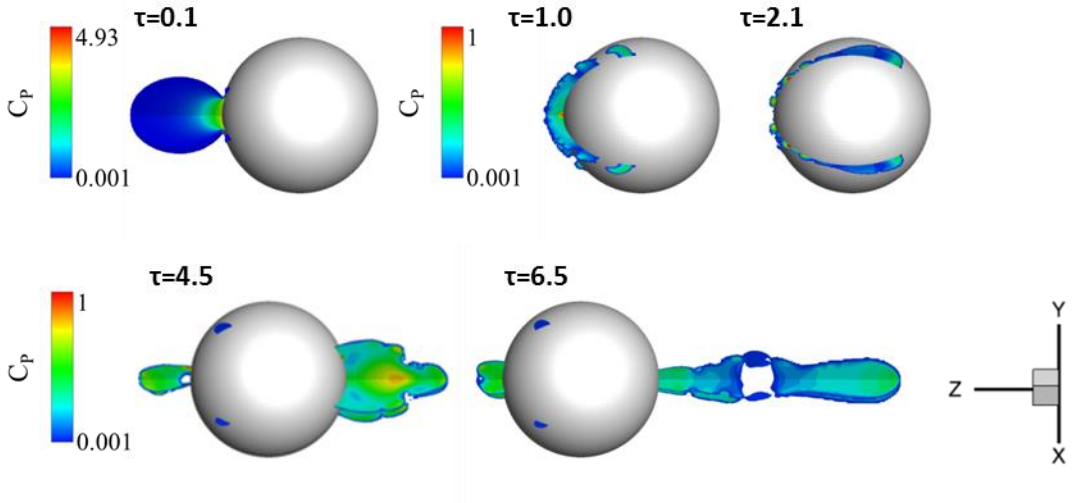

Figure 15. Temporal evolution of C_p for Case5 (DTP=0.62_We=40) at slices x=0 and y=0.

When the droplet impinges onto the solid particle, Cp rises up to almost 5 times the initial droplet impact kinetic energy, similar to the case of droplet impingement onto flat surfaces. At later stages corresponding to time instances of coating and formation of liquid ligaments, the liquid maximum pressure decreases. The liquid volume weighted velocity for Cases 4-9 is presented in Figure 16. In Case 4 the droplet rebounds from the solid particle, as it can be observed by the negative recoiling velocity in Figure 16a, while in all other cases the droplet coats the solid particle. It can be noticed that in cases 5,6 and cases 8,9, as We number increases, the average non-dimensional liquid velocity value follows a very similar trend; For cases 8 and 9, towards the later stages of the phenomenon stabilizes at values around 0.5-0.8 of the impact velocity.

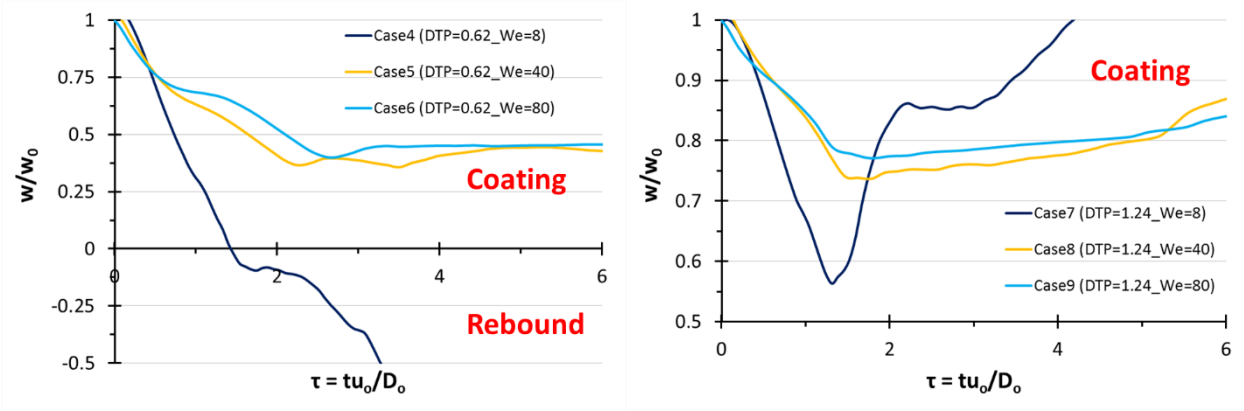

a. **b.**

Figure 16. Effect of We number on the liquid phase mean velocity along the drop-particle axis (z direction) for a) Cases4-6 and b) Cases7-9.

Another aspect which is worth mentioning is the maximum liquid film thickness at the point of impact as predicted by the numerical model. In Figure 17a, the definition of the film thickness measurement is presented, while in Figure 17b-d, this thickness is shown for all cases examined. The temporal evolution of the film thickness, as proposed by Bakshi et al. [11] can be separated in 3 phases, namely (a) the initial drop deformation phase, (b) the inertia dominated phase and (c) the viscosity dominated one. Phases 1

and 2 theoretical approximations are compared against the calculated values in Figure 17, in order to investigate the spreading process.

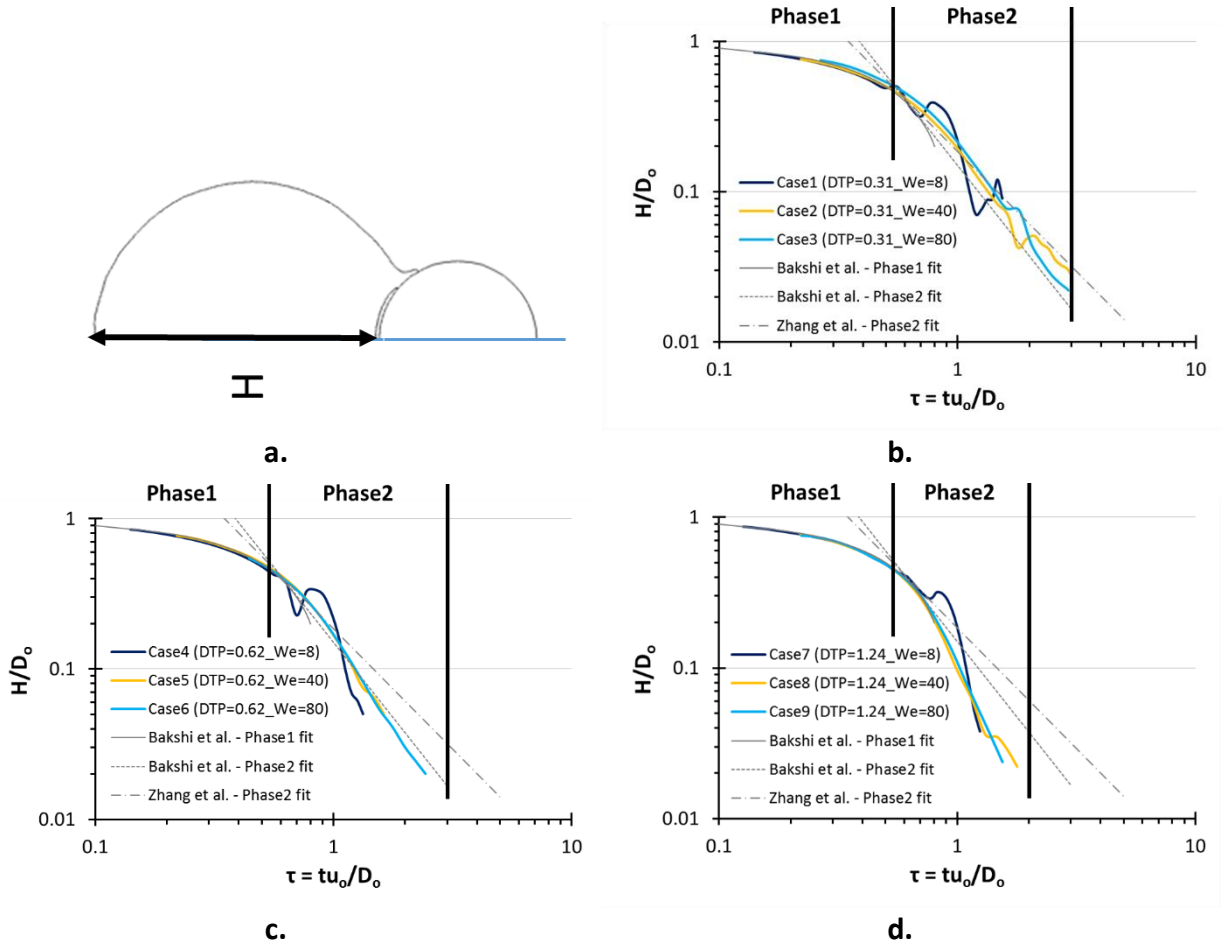

Figure 17. a) Definition of film thickness calculation at impact point, b, c, d) predicted non-dimensional film-thickness for cases 1-3, 4-6 and 7-9, respectively.

For phase 1, Bakshi et al. [11] proposed that the non-dimensional liquid thickness is correlated to non-dimensional time by the simple equation $\mathbf{H/D_0 = 1-\tau}$. This is in agreement with Zhang et al. [16] work, that have used Lattice-Boltzmann simulations to predict droplet impact. As presented by the current results, the same phase 1 trends are identified to fit well with this correlation. During phase 2, which is the inertia dominated period, the correlation proposed by Bakshi et al. [11] is $\mathbf{H/D_0 = 1.5/\tau^2}$. On the contrary, Zhang et al. [16] simulations indicated the relation $\mathbf{H/D_0 = 1.85/\tau^{1.6}}$. In this work, it is clear that all film thickness curves follow a similar trend for phase 2; however the slope of these curves varies with respect to the examined DTP value. For the lowest DTP value (0.31) examined in cases 1-3, the correlation given by Zhang et al. [16] is the closer one compared to the present results. Increasing the DTP value to 0.62, results in a more steep liquid thickness decrease, which is closer to the Bakshi et al. [11] fit. For the highest value of the DTP (1.24), phase2 is shorter, as it lasts for 2 units of non-dimensional time, while the slope is steeper than the one predicted by the aforementioned correlations. This is also shown in the work of Bakshi et al [11] (Figure 15 in their work), where the authors proposed different film thickness decrease slopes for different values of DTP using an analytical model for the prediction of the film flow. Their observations is thus predicted in this study using CFD analysis.

4.2.2 *Solid wetting area*

In this section the interest is turned towards the solid area percentage covered by liquid. This investigation may aid engineering areas where maximization/minimization of contact between liquid droplets and solid particles is needed. In Figure 18, the effect of the parameters investigated in this study (We, DTP) on the drop-particle wetting area is presented. Wetting area, is defined as the percentage of total particle area covered by liquid. This is calculated by the following equation:

$$wetting\ area = \frac{liquid\ area}{total\ area} = \frac{\sum_{wallf,\alpha>0.5} \alpha \cdot A_f}{\sum_{wallf} A_f} \qquad (7)$$

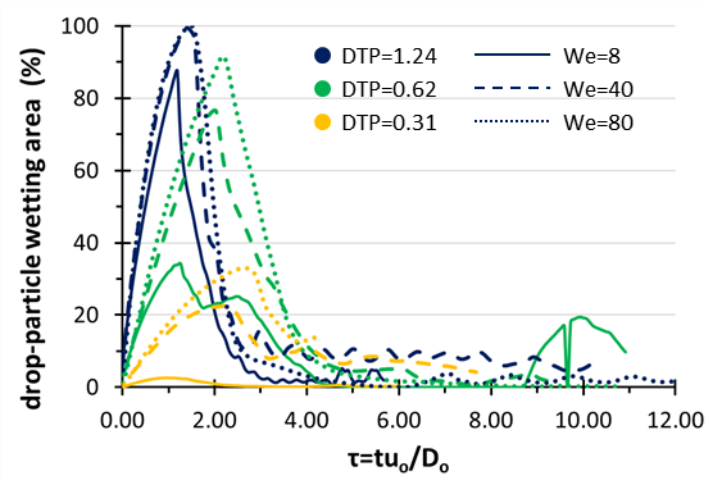

Figure 18. Temporal evolution of drop-particle wetting area coverage for cases 1-9 (We=8-80 and DTP=0.31-1.24).

It is clear that as the particle gets smaller, i.e. DTP gets higher, particle coating gets more intense. For the smallest particle (DTP=1.24), the percentage of particle area, which is covered by liquid mass is above 80%, not only for very low, but also for moderate Weber number impacts. Therefore, high DTP values promote solid-liquid contact. Moreover, for these impacts (DTP>0.6, Cases4-9), it is observed that the total contact time is almost the same, regardless of the collision outcome. For lower DTP values, liquid-solid contact area is less. As it is shown in Figure 9, when colliding with large particles, the droplet rebounds just as it would do on a flat surface.

5. Conclusions

This paper presents three-dimensional simulations of liquid droplet impact onto solid particles where the parameters under investigation were the We number and the droplet to particle size ratio (DTP). The results of such an investigation with the use of the VOF methodology along with adaptive local grid refinement have allowed evaluation of the effect of these parameters on the dynamics of the droplet spreading and the final outcome of collision. Though the investigation is limited to low viscous liquids (water) and a limited range of We and DTP numbers, important information on the possible outcome of such impacts has been extracted. Partial or full droplet rebound is promoted with very low We number and high DTP values, compared to the case of full particle coating when these values are increased. From the droplet dynamics point of view, the inertial forces dominate over the viscous, gravitational and surface

tension forces at the early stages of impact, while subsequently the role of wetting forces, surface tension, gravity and viscosity seem to play an important role, as in the case of droplet impingement onto flat surfaces. The non-dimensional film thickness throughout the phenomenon was predicted and found in good agreement with previous experimental and numerical studies. Moreover, it is shown that for high Weber number values (>40) and low DTP values (<0.62) the mean velocity of the liquid mass that leaves the particle after its coating is between 0.5-0.8 times the droplet initial impact velocity.

6. Acknowledgements

The present work was funded by the Marie Curie Fellowship (FP7-PEOPLE-2012-IEF) with Grant Agreement number 329500 funded by the European Commission entitled as "Non Flat Impingement—Droplet Impingement on Non-flat Surfaces".

7. References

1. Antonini, C., A. Amirfazli, and M. Marengo, *Drop impact and wettability: From hydrophilic to superhydrophobic surfaces.* Physics of Fluids, 2012. **24**(10): p. 102104-13.
2. Rein, M., *Phenomena of liquid drop impact on solid and liquid surfaces.* Fluid Dynamics Research, 1993. **12**(2): p. 61-93.
3. Rioboo, R., M. Marengo, and C. Tropea, *Time evolution of liquid drop impact onto solid, dry surfaces.* Experiments in Fluids, 2002. **33**(1): p. 112-124.
4. Yarin, A.L., *DROP IMPACT DYNAMICS: Splashing, Spreading, Receding, Bouncing.* Annual Review of Fluid Mechanics, 2006. **38**(1): p. 159-192.
5. Bayer, I.S. and C.M. Megaridis, *Contact angle dynamics in droplets impacting on flat surfaces with different wetting characteristics.* Journal of Fluid Mechanics, 2006. **558**: p. 415-449.
6. Chandra, S. and C.T. Avedisian, *On the Collision of a Droplet with a Solid Surface.* Proceedings of the Royal Society of London. Series A: Mathematical and Physical Sciences, 1991. **432**(1884): p. 13-41.
7. Pasandideh-Fard, M., et al., *Splat shapes in a thermal spray coating process: Simulations and experiments.* Journal of Thermal Spray Technology, 2002. **11**(2): p. 206-217.
8. Levin, Z. and P.V. Hobbs, *Splashing of Water Drops on Solid and Wetted Surfaces: Hydrodynamics and Charge Separation.* Philosophical Transactions of the Royal Society of London. Series A, Mathematical and Physical Sciences, 1971. **269**(1200): p. 555-585.
9. Hardalupas, Y., A.M.K.P. Taylor, and J.H. Wilkins, *Experimental investigation of sub-millimetre droplet impingement on to spherical surfaces.* International Journal of Heat and Fluid Flow, 1999. **20**(5): p. 477-485.
10. Gunjal, P.R., V.V. Ranade, and R.V. Chaudhari, *Experimental and computational study of liquid drop over flat and spherical surfaces.* Catalysis Today, 2003. **79–80**(0): p. 267-273.
11. Bakshi, S., I.V. Roisman, and C. Tropea, *Investigations on the impact of a drop onto a small spherical target.* Physics of Fluids (1994-present), 2007. **19**(3): p. -.
12. Ge, Y. and L.-S. Fan, *Droplet–particle collision mechanics with film-boiling evaporation.* Journal of Fluid Mechanics, 2007. **573**: p. 311-337.
13. Bangonde, S., P. Nikure, and V.V. Buwa, *Numerical Simulations of Dynamics of Drop Impact and Spreading on Cylindrical and Spherical Surfaces.* Presented at GLS-9/8th

World Congress of Chemical Engineering held at Montreal, Canada (August 23-27), 2009.
14. Gac, J.M. and L. Gradoń, *Lattice-Boltzmann modeling of collisions between droplets and particles.* Colloids and Surfaces A: Physicochemical and Engineering Aspects, 2014. **441**(0): p. 831-836.
15. Mitra, S., et al., *Droplet impact dynamics on a spherical particle.* Chemical Engineering Science, 2013. **100**(0): p. 105-119.
16. Zhang, D., K. Papadikis, and S. Gu, *Application of a high density ratio lattice-Boltzmann model for the droplet impingement on flat and spherical surfaces.* International Journal of Thermal Sciences, 2014. **84**(0): p. 75-85.
17. Malgarinos, I., et al., *VOF simulations of the contact angle dynamics during the drop spreading: Standard models and a new wetting force model.* Advances in Colloid and Interface Science, 2014. **212**(0): p. 1-20.
18. Hirt, C.W. and B.D. Nichols, *Volume of fluid (VOF) method for the dynamics of free boundaries.* Journal of Computational Physics, 1981. **39**(1): p. 201-225.
19. FLUENT, *User's Guide, version 14.5.* ANSYS Inc., 2011.
20. Ubbink, O., *Numerical prediction of two fluid systems with sharp interfaces*, 1997, Imperial College.
21. Nikolopoulos, N., K.S. Nikas, and G. Bergeles, *A numerical investigation of central binary collision of droplets.* Computers & Fluids, 2009. **38**(6): p. 1191-1202.
22. Nikolopoulos, N., A. Theodorakakos, and G. Bergeles, *Normal impingement of a droplet onto a wall film: a numerical investigation.* International Journal of Heat and Fluid Flow, 2005. **26**(1): p. 119-132.
23. Nikolopoulos, N., A. Theodorakakos, and G. Bergeles, *Three-dimensional numerical investigation of a droplet impinging normally onto a wall film.* Journal of Computational Physics, 2007. **225**(1): p. 322-341.
24. Nikolopoulos, N., A. Theodorakakos, and G. Bergeles, *A numerical investigation of the evaporation process of a liquid droplet impinging onto a hot substrate.* International Journal of Heat and Mass Transfer, 2007. **50**(1–2): p. 303-319.
25. Strotos, G., et al., *Non-dimensionalisation parameters for predicting the cooling effectiveness of droplets impinging on moderate temperature solid surfaces.* International Journal of Thermal Sciences, 2011. **50**(5): p. 698-711.
26. Strotos, G., et al., *Numerical investigation of the cooling effectiveness of a droplet impinging on a heated surface.* International Journal of Heat and Mass Transfer, 2008. **51**(19–20): p. 4728-4742.
27. Strotos, G., et al., *Numerical investigation on the evaporation of droplets depositing on heated surfaces at low Weber numbers.* International Journal of Heat and Mass Transfer, 2008. **51**(7–8): p. 1516-1529.
28. Strotos, G., et al., *Cooling effectiveness of droplets at low Weber numbers: Effect of temperature.* International Journal of Thermal Sciences, 2013. **72**(0): p. 60-72.
29. Elias, R.N., M.A. Martins, and A.L. Coutinho, *Simple finite element-based computation of distance functions in unstructured grids.* International journal for numerical methods in engineering, 2007. **72**(9): p. 1095-1110.
30. Roisman, I.V., et al., *Drop impact onto a dry surface: Role of the dynamic contact angle.* Colloids and Surfaces A: Physicochemical and Engineering Aspects, 2008. **322**(1–3): p. 183-191.
31. Sikalo, S., et al., *Dynamic contact angle of spreading droplets: Experiments and simulations.* Physics of Fluids, 2005. **17**(6): p. 062103-13.

32. Pasandideh-Fard, M., S. Chandra, and J. Mostaghimi, *A three-dimensional model of droplet impact and solidification.* International Journal of Heat and Mass Transfer, 2002. **45**(11): p. 2229-2242.
33. Bussmann, M., J. Mostaghimi, and S. Chandra, *On a three-dimensional volume tracking model of droplet impact.* Physics of Fluids (1994-present), 1999. **11**(6): p. 1406-1417.
34. Gumulya, M., et al., *Evaporation of a droplet on a heated spherical particle.* Chemical Engineering Journal, 2015. **278**: p. 309-319.
35. Thoroddsen, S., T. Etoh, and K. Takehara, *Air entrapment under an impacting drop.* Journal of Fluid Mechanics, 2003. **478**: p. 125-134.
36. Bouwhuis, W., et al., *Maximal Air Bubble Entrainment at Liquid-Drop Impact.* Physical Review Letters, 2012. **109**(26): p. 264501.